Supplementary Materials

Bubble Wrap-like Carbon-Coated Rattle-Type silica@silicon Nanoparticles as Hybrid Anode Materials for Lithium-Ion Batteries via Surface-Protected Etching

Angelica Martino [1], Jiyun Jeon [2], Hyun-Ho Park [1], Hochun Lee [2], and Chang-Seop Lee [1,*]

[1]Department of Chemistry, Keimyung University, Daegu 42601, Republic of Korea
angelicamartino97@kmu.kr (A.M.); rubchem@kmu.ac.kr (H.-H.P.)

[2]Department of Energy Science and Engineering, DGIST, Daegu 42988, Republic of Korea
jiyunn1234@dgist.ac.kr (J.J.); dukelee@dgist.ac.kr (H.L.)

*Corresponding author: Chang-Seop Lee

Department of Chemistry, Keimyung University, Daegu 42601, Republic of Korea

Phone No: +82-53-580-5192; Fax No: +82-53-580-5056

E-mail: surfkm@kmu.ac.kr

List of Figures

List of Tables

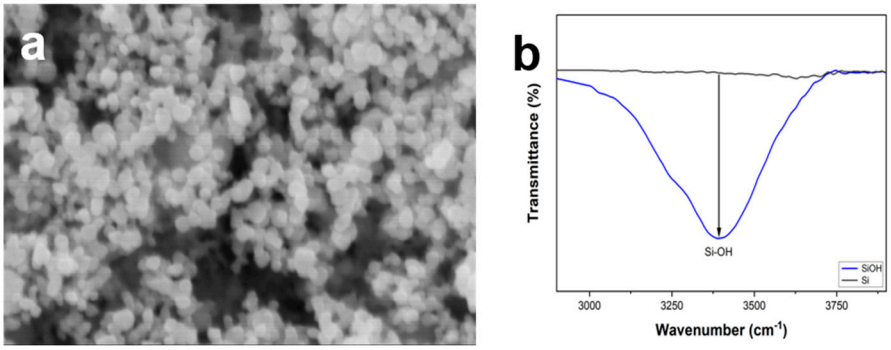

Figure S1. FE-SEM image of (a) pure Si nanoparticles. (b) FT-IR result comparing pure Si nanoparticles and Si–OH after piranha solution pre-treatment.

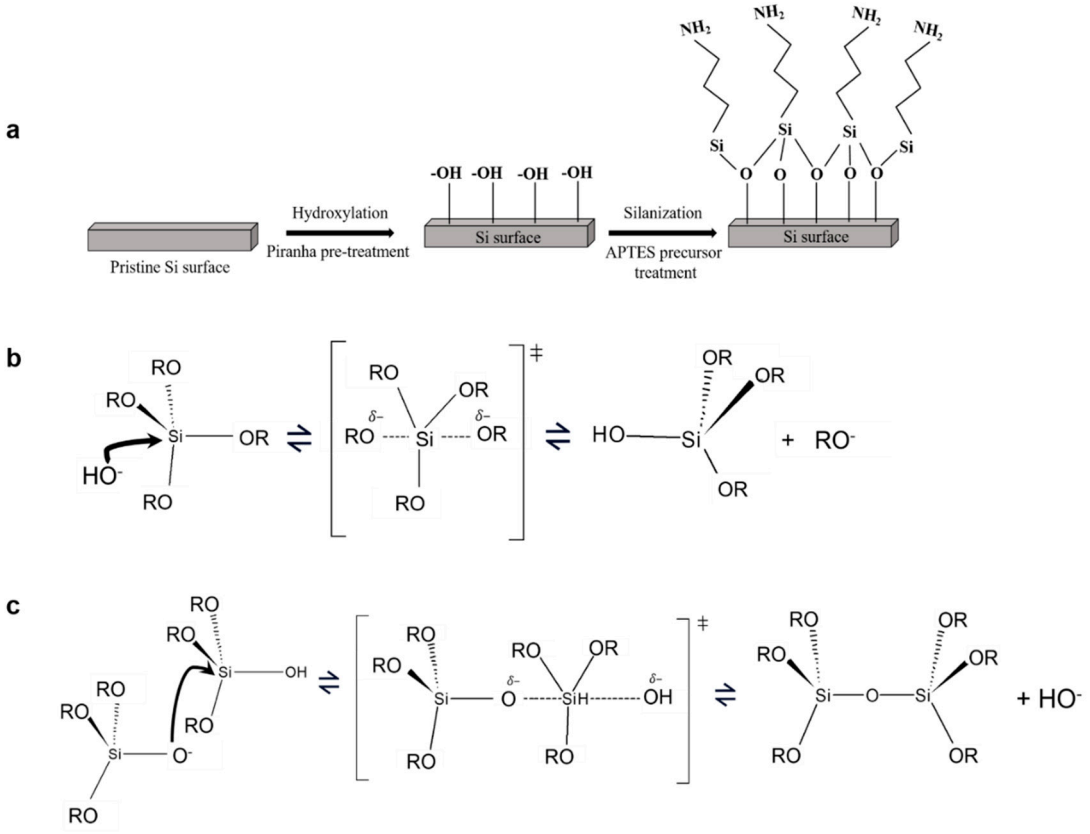

Figure S2. (a) Formation of siloxane networks from piranha-treated Si–OH using APTES. (b) Hydrolysis and (c) condensation reaction mechanism of TEOS showing formation of siloxane bridges.

Hydrolysis Reaction:

APTES reacts with water, leading to the hydrolysis of the ethoxysilane groups. This results in the formation of hydroxyl-modified APTES and ethanol. The presence of hydroxyl groups on APTES is crucial for subsequent condensation reactions.

Condensation:

Hydroxyl-modified APTES undergoes condensation reactions, forming siloxane bonds on the silica surface. This step contributes to the growth of the silica network.

Self-catalysis:

Siloxane bonds formed on the silica surface can undergo self-catalysis. In this process, water molecules react with the siloxane bonds, regenerating hydroxyl groups on the silica surface and releasing a hydroxyl-modified APTES.

This self-catalysis step contributes to the continual growth of the silica nanoparticles and ensures the presence of hydroxyl groups on the surface.

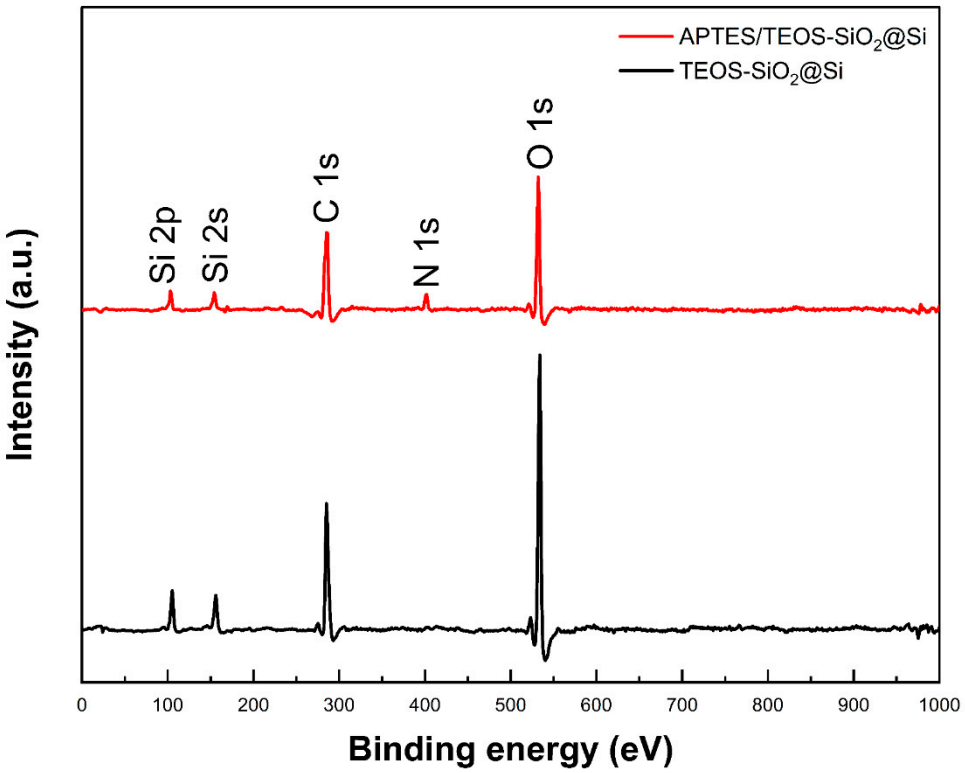

Figure S3. XPS survey scan of TEOS–SiO_2@Si and APTES/TEOS–SiO_2@Si precursors.

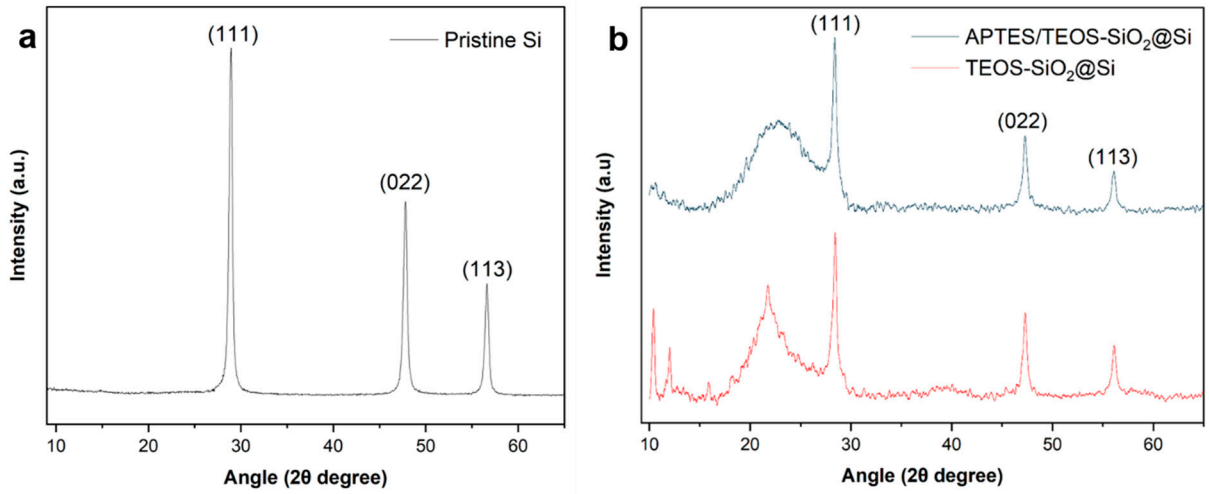

Figure S4. XRD patterns of (a) Si and (b) TEOS-derived SiO_2@Si and APTES/TEOS-derived SiO_2@Si.

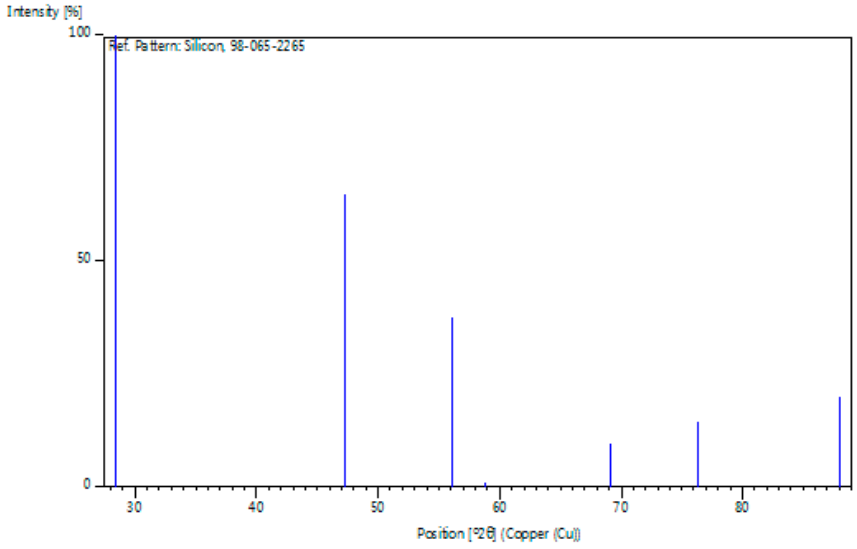

Figure S5. XRD reference peaks for face-centered cubic Si crystal (Reference code 98-065-2265)

Peak list

No.	h	k	l	d [Å]	2Theta[deg]	I [%]
1	1	1	1	3.13559	28.442	100.0
2	0	2	2	1.92015	47.302	65.0
3	1	1	3	1.63751	56.122	37.8
4	2	2	2	1.56779	58.856	0.0
5	0	0	4	1.35775	69.129	9.8
6	1	3	3	1.24596	76.375	14.4
7	2	2	4	1.10860	88.029	19.9

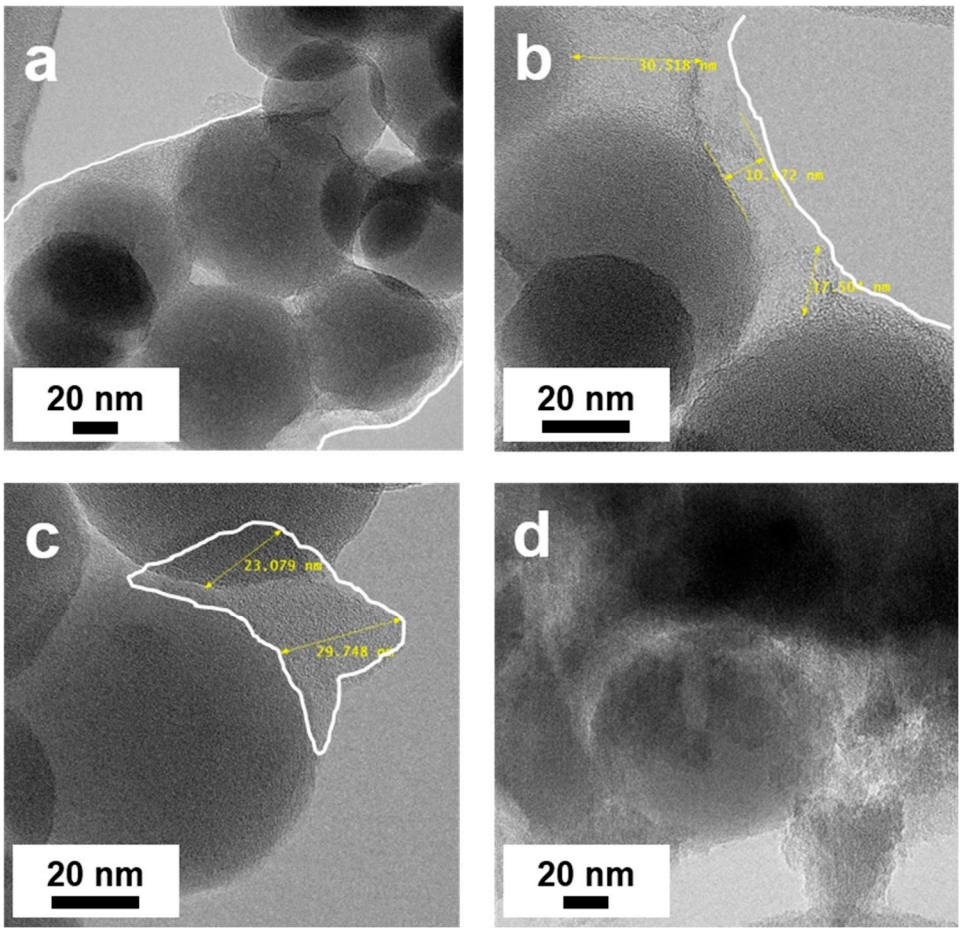

Figure S6. TEM images showing carbon crosslinking from PEI and PDA carbon coating efficiency in (a, b) composite samples prepared via traditional SiO_2 sol-gel synthesis reaction and carbon coating at room temperature and (c, d) composite samples prepared via hydrothermal treatment at 140 ºC for 24 h.

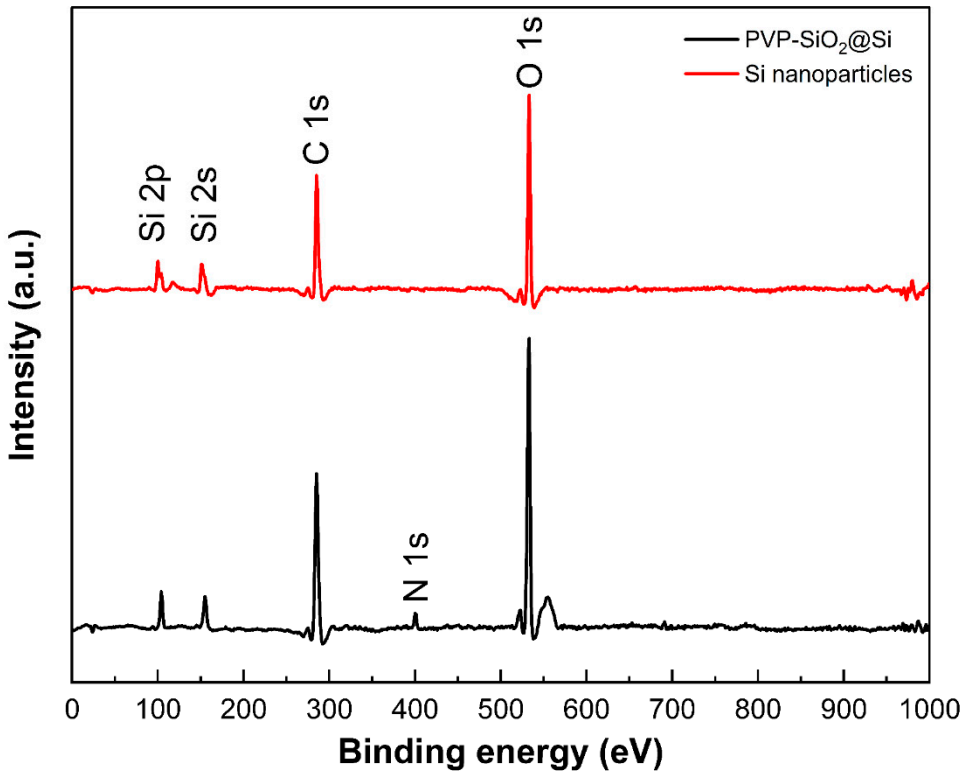

Figure S7. XPS survey spectra of PVP–SiO_2@Si and Si nanoparticles.

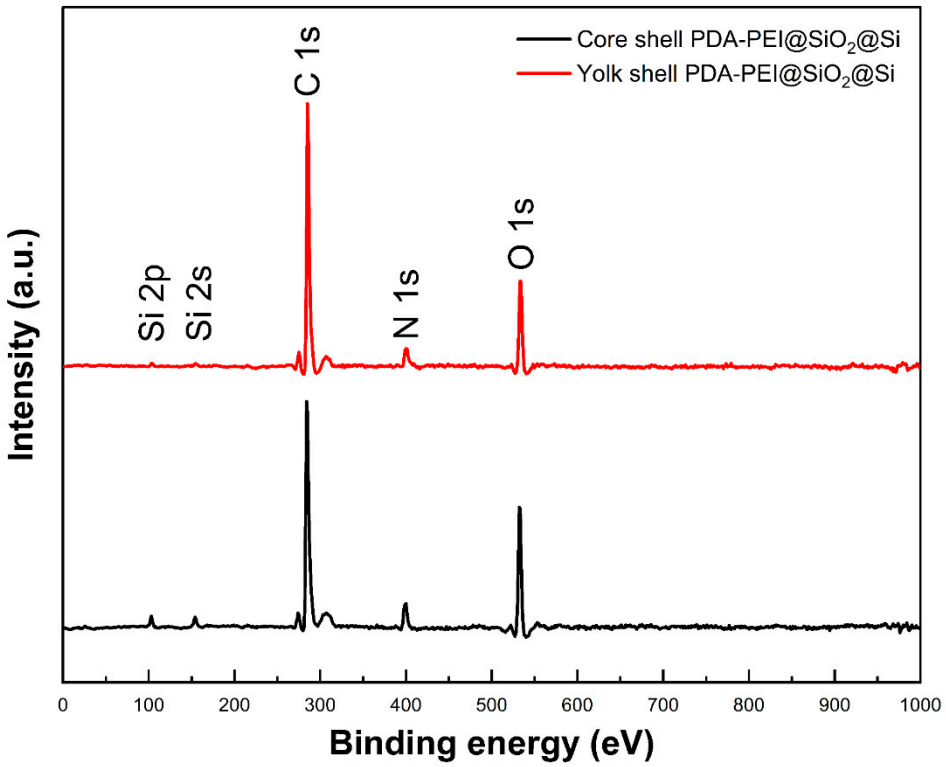

Figure S8. XPS survey spectra core shell PDA–PEI@SiO_2@Si and yolk shell PDA–PEI@SiO_2@Si composite samples.

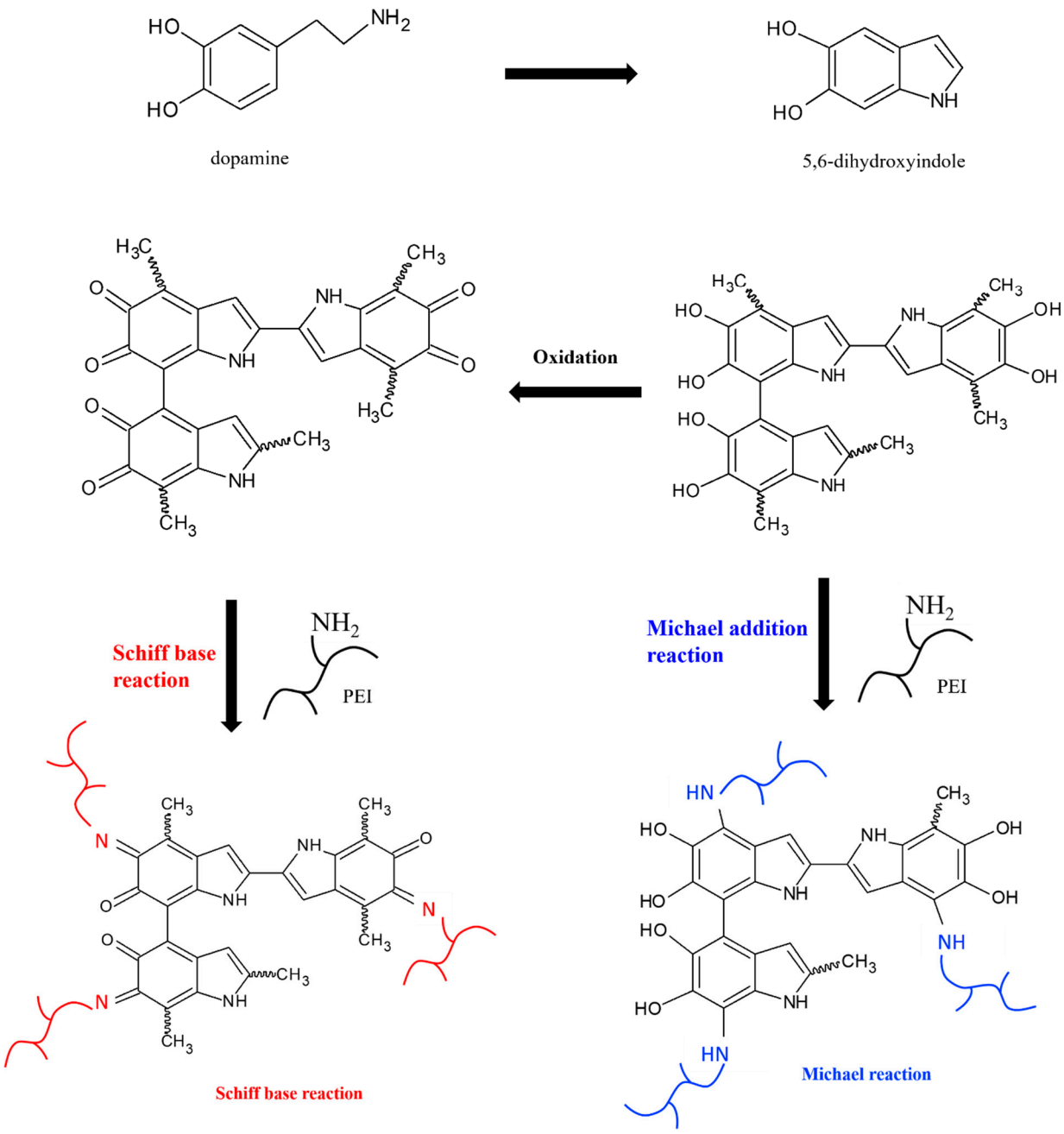

Figure S9. Illustration of the two possible reaction mechanisms showing the formation of PDA–PEI carbon crosslinks.

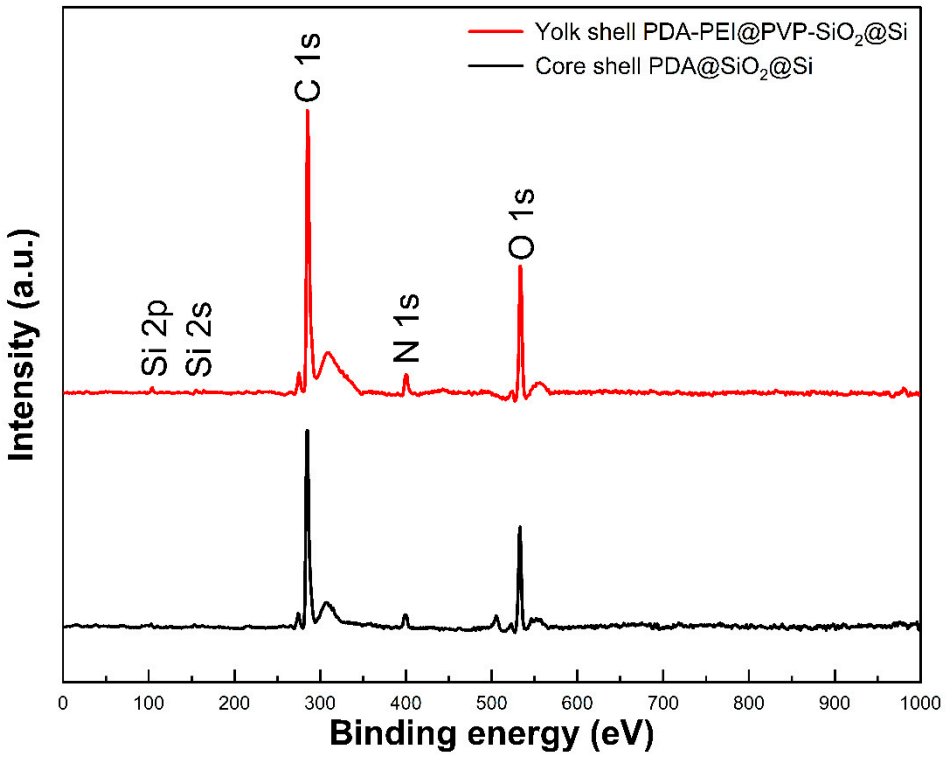

Figure S10. XPS survey spectra core shell PDA@SiO_2@Si and yolk shell PDA–PEI@PVP–SiO_2@Si composite samples.

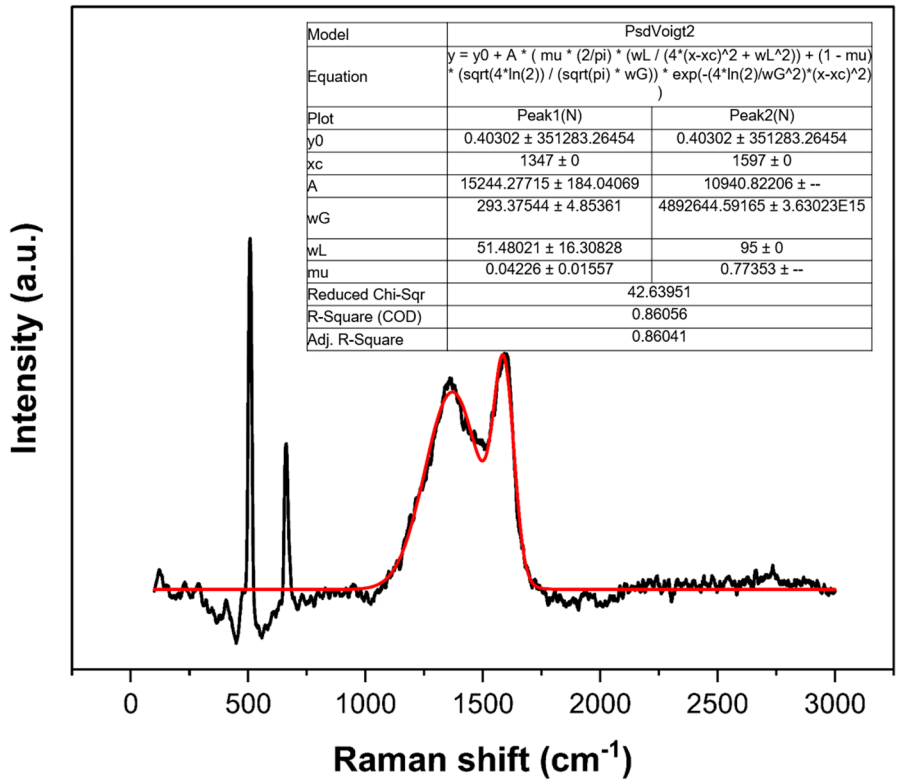

Figure S11. Raman peak fitting of core shell PDA@SiO_2@Si composite sample.

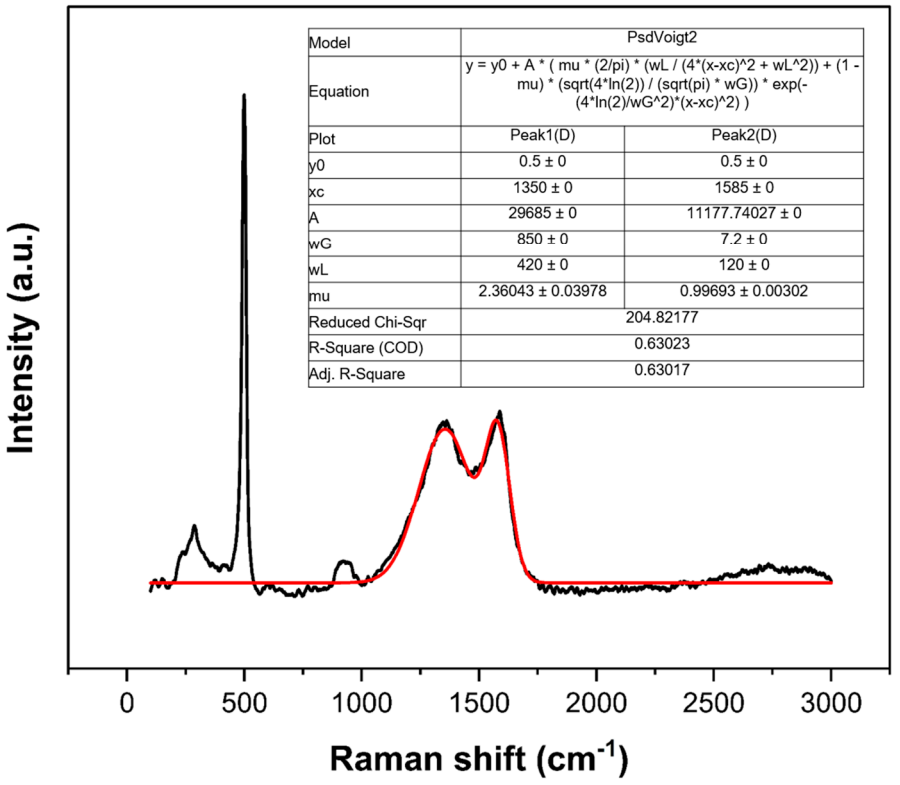

Figure S12. Raman peak fitting of yolk shell PDA–PEI@SiO_2@Si composite sample.

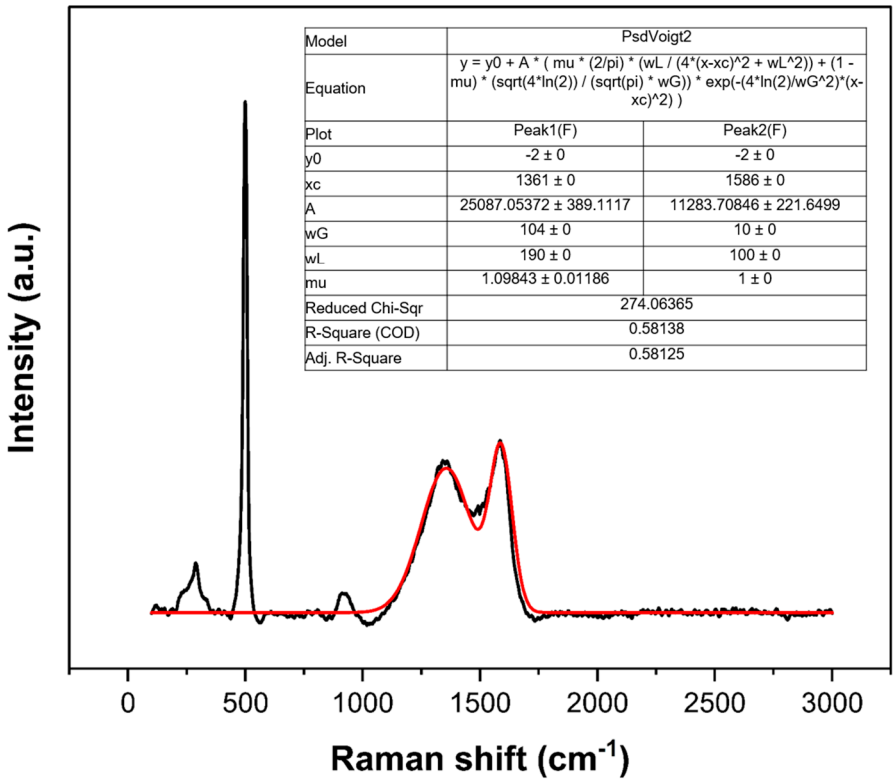

Figure S13. Raman peak fitting of yolk shell PDA–PEI@PVP–SiO_2@Si composite sample.

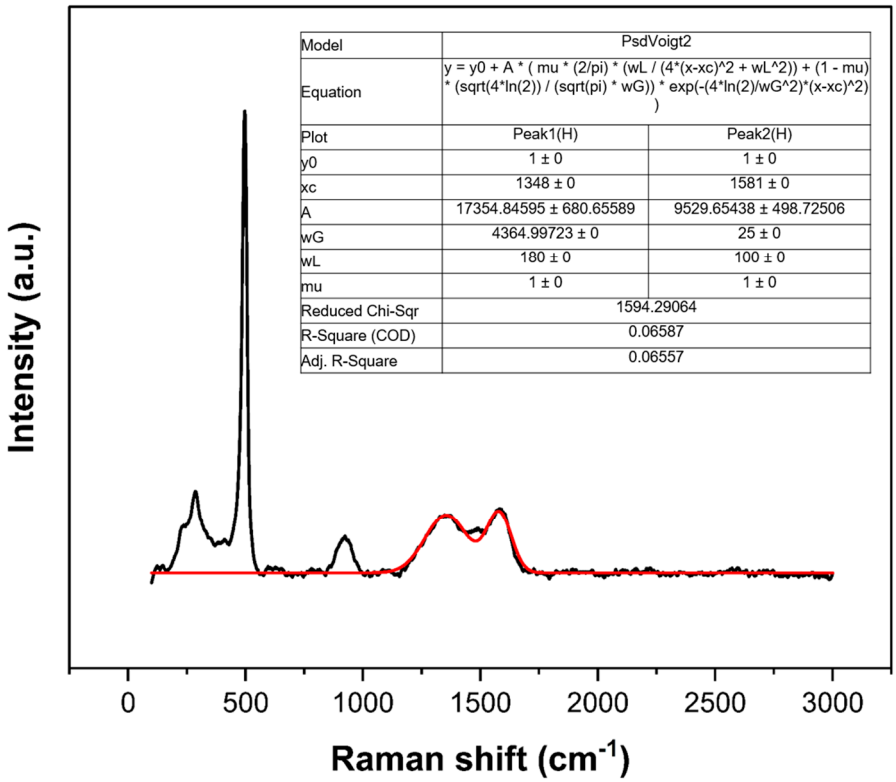

Figure S14. Raman peak fitting of core shell PDA–PEI@SiO_2@Si composite sample.

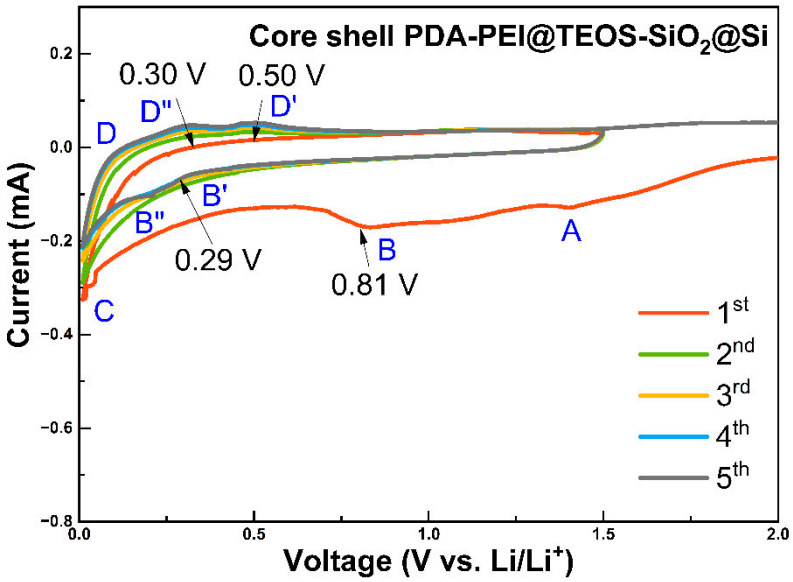

Figure S15. CV scans of core shell PDA–PEI@TEOS–SiO_2@Si composite fabricated via RT using TEOS as precursor solution.

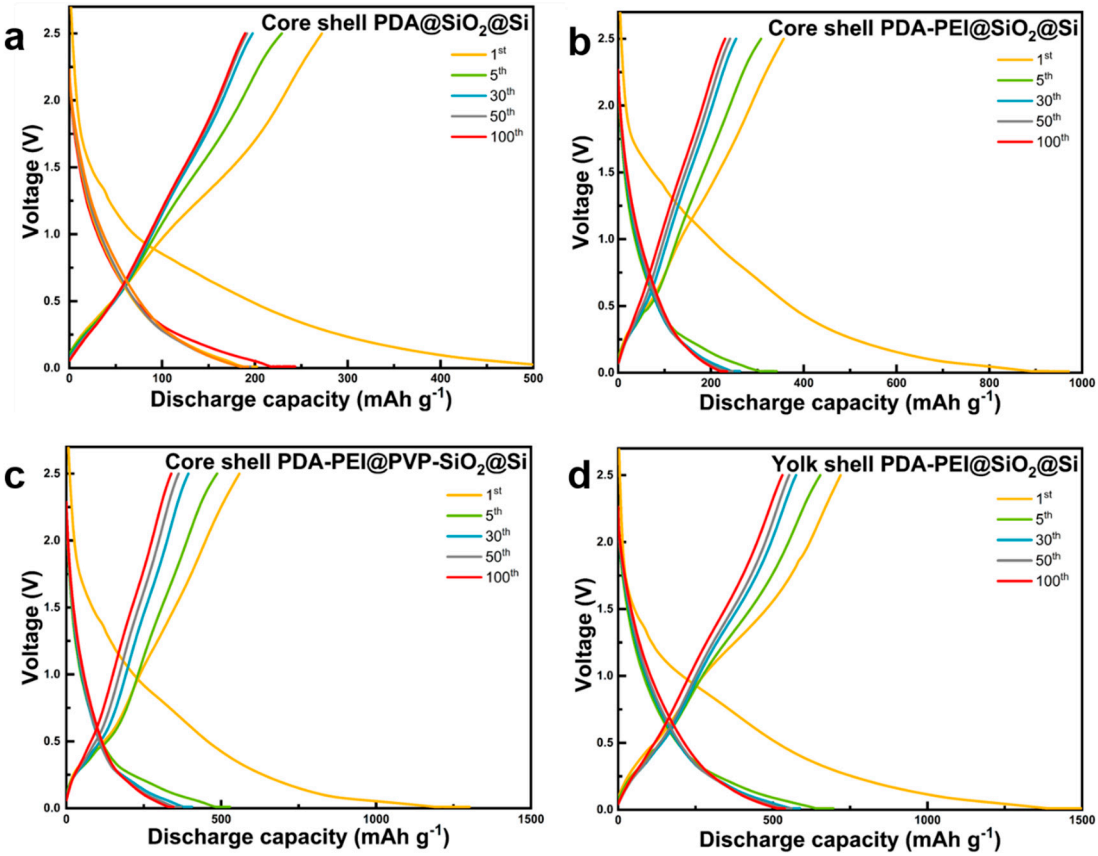

Figure S16. Galvanostatic charge and discharge profiles of core shell PDA@SiO_2@Si (a), core shell PDA–PEI@SiO_2@Si (b), core shell PDA–PEI@PVP–SiO_2@Si (c), and yolk shell PDA–PEI@SiO_2@Si (d) composite samples.

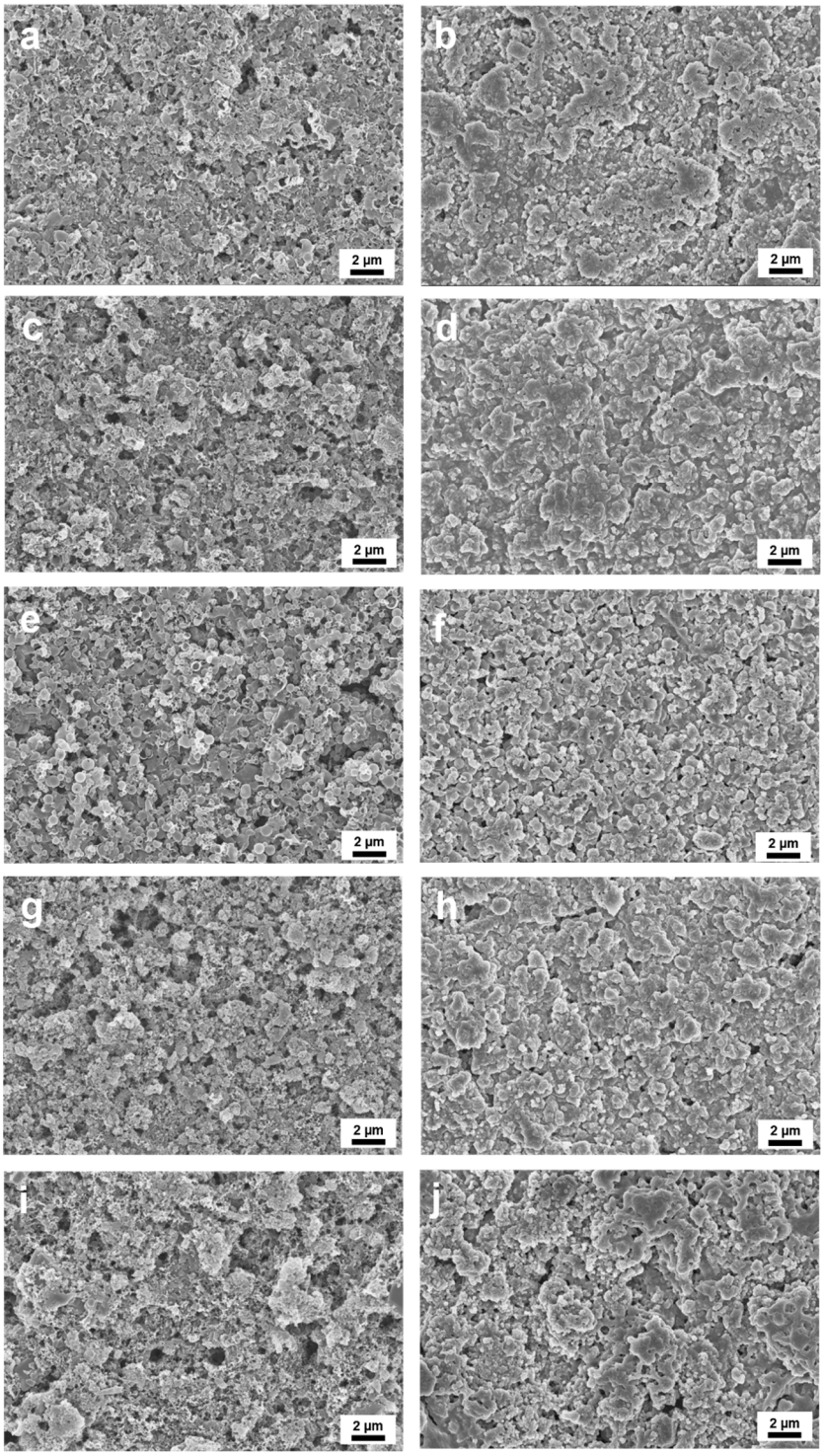

Figure S17. Representative SEM images showing the surface morphology of particles in (a, b) yolk shell PDA–PEI@PVP–SiO_2@Si, (c, d) yolk shell PDA–PEI@SiO_2@Si, (e, f) core shell PDA–PEI@PVP–SiO_2@Si, (g, h) core shell PDA–PEI@SiO_2@Si, and (i, j) core shell PDA@SiO_2@Si anode (a, c, e, g, i) before and (b, d, f, h, j) after 200 lithiation/delithiation cycles at 1 A g^{-1} current density.

Table S1. The I_D/I_G values of the samples calculated by the ratio of the D band peak area to the G band peak area using Gaussian–Lorentzian curve fitting model.

Sample	D band			G band			I_D/I_G
	A	I	FWHM	A	I	FWHM	
Core shell PDA@SiO_2@Si	15244.277	1347.0	51.480	10940.822	1597.0	95.0	0.84
Yolk shell PDA–PEI@SiO_2@Si	29685.0	1350.0	420.0	11177.740	1585.0	120.0	0.85
Yolk shell PDA–PEI@PVP–SiO_2@Si	25087.054	1361.0	190.0	11283.708	1586.0	100.0	0.86
Core shell PDA–PEI@SiO_2@Si	17354.846	1348.0	180.0	9529.654	1581.0	100.0	0.85

Table S2. The porous structure of the representative composite samples described by BJH model of BET analysis.

Sample	S_{BET} (m^2 g^{-1})	S_{me}* (m^2 g^{-1})	S_{mi}* (m^2 g^{-1})	V_t* (cm^3 g^{-1})
Core shell PDA@SiO_2@Si	224.56	149.66	177.42	0.48
Core shell PDA–PEI@SiO_2@Si	226.40	163.77	202.59	0.65
Core shell PDA–PEI@PVP–SiO_2@Si	409.05	219.13	337.65	0.67
Yolk shell PDA–PEI@SiO_2@Si	589.83	321.92	610.43	0.13
Yolk shell PDA–PEI@PVP–SiO_2@Si	654.63	570.96	519.09	0.12

*S_{me}, specific surface area of the mesopores; S_{mi}, specific surface area of the micropores; V_t, the total pore volume.